

Deep Phasor Networks: Connecting Conventional and Spiking Neural Networks

Wilkie Olin-Ammentorp^{1,2}, Maxim Bazhenov^{1,2*}

1 Department of Medicine, University of California, San Diego

2 Institute for Neural Computation, University of California, San Diego

* Correspondence:

Maxim Bazhenov

mbazhenov@health.ucsd.edu

Abstract:

In this work, we extend standard neural networks by building upon an assumption that neuronal activations correspond to the angle of a complex number lying on the unit circle, or ‘phasor.’ Each layer in such a network produces new activations by taking a weighted superposition of the previous layer’s phases and calculating the new phase value. This generalized architecture allows models to reach high accuracy and carries the singular advantage that mathematically equivalent versions of the network can be executed with or without regard to a temporal variable. Importantly, the value of a phase angle in the temporal domain can be sparsely represented by a periodically repeating series of delta functions or ‘spikes’. We demonstrate the atemporal training of a phasor network on standard deep learning tasks and show that these networks can then be executed in either the traditional atemporal domain or spiking temporal domain with no conversion step needed. This provides a novel basis for constructing deep networks which operate via temporal, spike-based calculations suitable for neuromorphic computing hardware.

Introduction:

Efficient learning and inference processes remain a challenge for deep-learning based artificial intelligence methods (1). The problems include poor generalization beyond properties of the training data (2), catastrophic forgetting during new task learning (3), lack of transfer of knowledge (4). Many efforts focus on addressing this by carrying out deep learning via the use of networks which communicate via binary events - ‘spikes,’ bringing artificial neurons closer to their highly efficient biological counterparts (5–7). While recent efforts to link traditional deep neural networks (DNNs) to spiking neural networks (SNNs) via the usage of rate-coding have yielded SNNs which can attain high accuracy, this achievement comes with several caveats. Firstly, converting a suitable DNN to a rate-based SNN can require complex conversion methods to normalize weights and activation values (8–10). Secondly, the resulting spike-based networks lack many established characteristics of biological computation, such as fast inference and sensitivity to the timing of individual spikes (11–15). Lastly, even when executing on specialized neuromorphic hardware, these spiking networks require processing long sequences of spikes to evaluate rate and as a result provide at best a marginal gain in energy efficiency when compared to traditional networks running on conventional hardware (16). For these reasons, to create a spiking network which can achieve the goals of neuromorphic computing (such as high performance, energy efficiency, and biological relevance), alternate approaches from rate-coding will likely be required (17–21).

We build on previous work that assumes the state of a neuron may be represented by the angle of a complex number, commonly referred to as a “phasor” (22,23). Phasors are often used in electrical engineering and physics to provide convenient representations and manipulations of sinusoidal signals with a common frequency (24). A phasor describes a sinusoidal signal’s phase offset relative to a reference signal, and can be scaled by a real magnitude to describe any complex number in polar form.

$$\text{Equation 1. } A\angle\varphi = Ae^{i(\omega t + \varphi)} = \cos(\omega t + \varphi) + i \sin(\omega t + \varphi)$$

Any set of sinusoidal signals with a common frequency can be represented by a vector of phasors, and as their superposition produces another sinusoid, it can also be represented by a single new phasor. This value is calculated by summing the original vector of phasors in their complex form. The phase of the resulting complex number is calculated via a non-linear trigonometric operation, allowing the superposition of phasors to form the basis of a neuronal activation function suitable for a deep neural network. The representation of information through phasors and non-linear properties of their superpositions provide the basis of information processing within phasor networks. While the apparent phase of a signal varies with respect to time, either an absolute starting time or reference signal can be used to decode phases from a set of time-varying signals.

In this work we propose an extension of the “classic” deep neural network architecture by replacing real-valued activation nodes by phasors. We describe the operations needed to calculate propagation of the activation through the phasor network and show that the phasor network can be executed either in an atemporal domain or temporal domain. In the former, values are passed between layers in standard tensors of real values. In the latter, values are passed between layers by series of precisely-timed spikes, referred to as ‘spike trains’. Atemporal execution is well-suited to existing compute architectures (e.g. CPU and GPU), and temporal execution is suited to current or future neuromorphic platforms. We demonstrate that either execution mode leads to similar performance on standard machine learning datasets.

Results:

Atemporal Evaluation

Activation Function

Let us assume that the input to a single neuron consists of a vector of phases, \mathbf{x} . For convenience and ease of integration within existing deep learning frameworks, in this work all phase angles are reported after being normalized by π , so that $\mathbf{x} \in [-1,1]$. Multiplying these values by π converts to a standard angle in radians.

To compute a single neuron’s output y given an input vector \mathbf{x} with n elements, the real valued phases \mathbf{x} are converted into an explicit complex representation. These complex elements are then scaled by a vector of corresponding weights \mathbf{w} , which we currently restrict to be entirely real-valued. The sum of the scaled complex elements produces a new complex value with an amplitude and phase (Equation 2). To extract only its phase, the two-argument arctangent (*atan2*) is applied (Equation 3). Through these operations, a nonlinear neuronal operation is obtained. Additionally, the local continuity of these operations ensures deep networks employing them can be optimize each neuron’s weights \mathbf{w} using standard backpropagation techniques.

$$\text{Equation 2. } x' = \sum_{i=1}^n e^{i\pi x_i}$$

$$\text{Equation 3. } y = \text{atan2}[\text{Im}(x'), \text{Re}(x')]$$

Output and Loss Functions

In an image classification task, the output of a standard network is often a vector of real values normalized between zero and one using the softmax function (25). The outputs of this network are then taken to be the probability that the input image belongs to the corresponding output class, and a loss function such as cross-entropy is used to minimize the divergence between the network’s predictions and the image’s ground-truth class.

In contrast, in a phasor network the output layer creates a vector of phases. Given an input image with a label c out of a total of n_c classes, the network predicts this class at the output by causing the corresponding neuron in the output layer to produce a phase which is in quadrature (90° out-of-phase) to all others (Equation 4). A loss function using cosine similarity of the vector of predicted values ($\hat{\mathbf{y}}$) to the target vector (\mathbf{y}) is used to measure the convergence of the network’s output to the desired phase encoding (Equation 5). For an input with an unknown label, the predicted class \hat{c} is produced by finding the neuron which produces a phase closest to 90° (Equation 6).

$$\text{Equation 4. } \mathbf{y} = \frac{1}{2} \cdot \text{onehot}(c, n_c)$$

$$\text{Equation 5. } \text{loss}(\mathbf{y}, \hat{\mathbf{y}}) = 1 - \cos[\pi \cdot (\mathbf{y} - \hat{\mathbf{y}})]$$

$$\text{Equation 6. } \hat{c} = \text{argmin}[\text{abs}(\hat{\mathbf{y}} - \frac{1}{2})]$$

Image-to-Phase Conversion

One issue in implementing phasor-based networks arises at the input layer of such a network. Inputs such as images are almost always encoded on a domain with pixel intensities normalized between 0 and 1. However, as previously stated, a phasor network utilizes inputs on the domain $[-1,1]$. We show below that an initial conversion step between domains can assist phasor networks in reaching performance levels that match conventional networks. A simple linear scaling ($2x - 1$) between domains is insufficient, as this will lead to ones and zeros being encoded into phases which have an identical cosine similarity (-1 and 1). Instead, we utilize two intensity-to-phase conversion methods: the first is a ‘normalized random projection’ (NRP), and the second a ‘random pixel phase’ (RPP).

The NRP method constructs a random projection by sampling values from a uniform distribution on the domain $[-1,1]$. The input image is then multiplied by this square matrix to produce a new input vector of the same dimension with pixel data distributed across multiple values. A simplified batch-normalization layer with two moving moments learned during training (mean and standard deviation) is applied to the random projection to keep approximately 99% of projected phases within the range $[-1,1]$. Lastly, outlier values are clipped to this domain.

The RPP method randomly chooses input pixels which are either multiplied by 1 or -1 . Collectively, this spreads values across the domain $[-1,1]$ although the absolute range of an individual pixel does not increase.

Model Architecture and Accuracy

To show that deep phasor networks can be effectively trained using the approach described above, we train a series of standard and phasor-based image classifiers on the standard MNIST, FashionMNIST, and CIFAR-10 datasets (26–28).

First, we demonstrate a simple multilayer-perceptron (MLP) model with one hidden layer. The architectures of the MLP networks trained on MNIST-format images ($28 \times 28 \times 1$ pixels) are identical, consisting of an input layer, intensity-to-phase conversion method, hidden layer of 100 neurons, and an

output layer of 10 neurons, with biases are disabled for all neurons. A neuronal dropout rate of 25% is used for regularization (Figure 1a). In the standard networks, a ReLU activation function is used, and in phasor networks, the previously described activation method is used.

In these results, we train groups of 12 models and report the group’s mean accuracy plus or minus its standard deviation. Phase projection layers are included even in standard networks as they can affect test accuracy, particularly for the MNIST dataset.

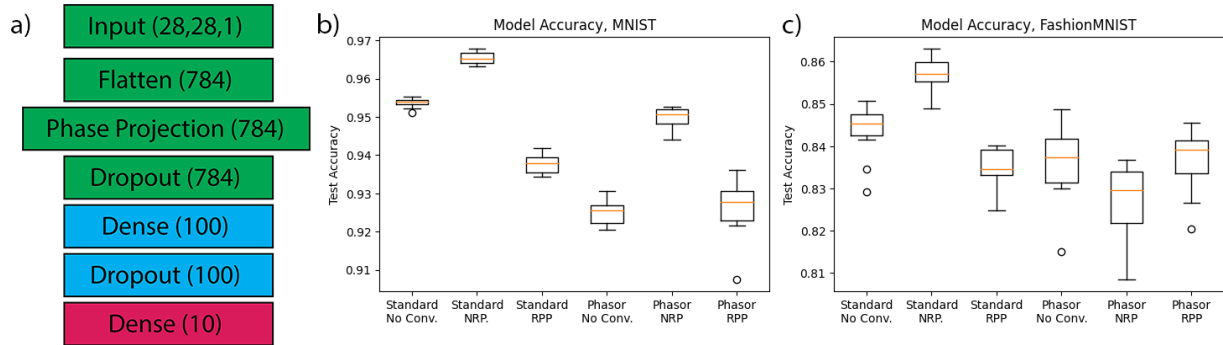


Figure 1: (a) Architecture of the networks used. Each layer is labeled with its output shape. (b) Classification accuracy of this model on the standard MNIST dataset and (c) FashionMNIST dataset over 12 trials. ‘Standard’ models use a ReLU activation function and phasor models use the phasor activation method described above. NRP models apply a normalized random projection to convert intensities to phases and RPP models randomly select pixels to produce positive or negative phases.

With an NRP conversion, the standard models reached a test accuracy of $96.4 \pm 0.1\%$ on standard MNIST after 2 epochs of training. Similarly, the phasor models reached a median accuracy of $95.0 \pm 0.3\%$. Training instead on FashionMNIST dataset, the standard models with NRP conversion reached $85.7 \pm 0.4\%$ accuracy on the test set. The highest-performing phasor networks for FashionMNIST used the RPP conversion, with an accuracy of $83.7 \pm 0.7\%$ (Figure 1).

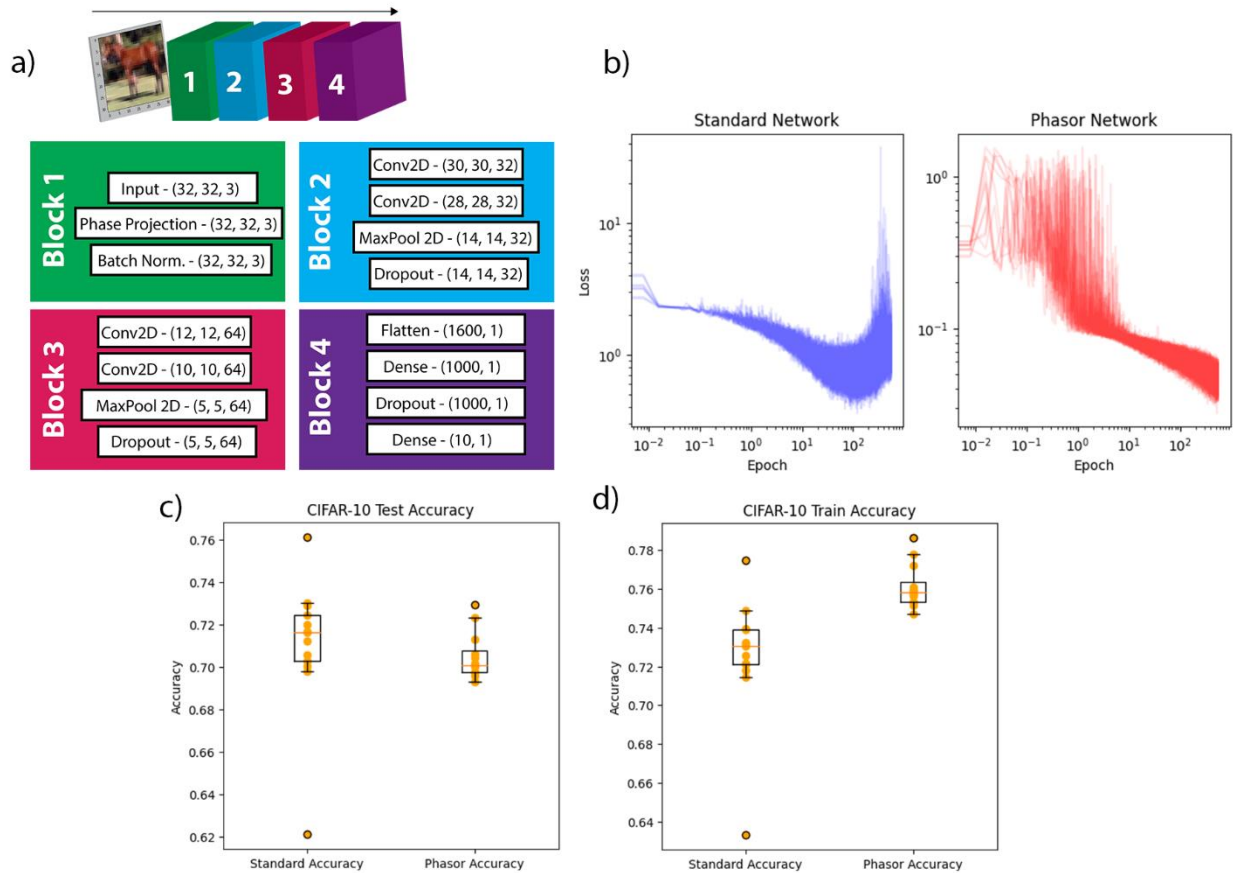


Figure 2: (a) Architecture used for the CIFAR-10 image classification task. This 15-layer network utilizes operations required for modern image classifiers such as convolutional layers and spatial pooling. This architecture is implemented with ReLU activation functions (except for a final softmax) to produce the standard network. In phasor networks, all layers use the phasor activation method and a minimum-pool operation is substituted, but the architecture otherwise remains the same. (b) Loss curves during network training show a common pattern for both network types, though the loss of the standard networks in later epochs is more greatly affected by the included L2 loss on convolutional kernel weights. (c) Phasor and standard networks reach the same classification accuracy on the test set (no significant difference, $p=0.58$, $n=12$). (d) There is a slight but significant difference in the accuracy on the training set, with phasor networks producing significantly higher accuracy ($p=0.001$, $n=12$).

To classify the CIFAR-10 dataset, a convolutional architecture is used. It consists of an input block, two convolutional blocks, and a dense output block (Figure 2a). The input block consists of an optional phase projection method followed by a batch-normalization step. The first convolutional block consists of two convolution layers with 32 channels and 3x3 kernels, followed by a 2x2 max-pool and 25% dropout. The second convolutional block is identical but uses convolutional layers with 64 channels. An additional L2 regularization is applied to kernels in all convolutional layers. The dense block flattens the convolutional output, and applies a dense layer with 1000 neurons, a dropout of 25%, and a final dense layer of 10 neurons. Biases are again disabled on all neurons. All layers in this standard model use a ReLU activation except for the final dense layer which uses a softmax. No phase projection is used for the standard network, and RPP is used for the phasor network.

In the CIFAR network, one additional change is made between standard and phasor-based networks. In the latter case, a minimum-pool (min-pool) is substituted for the more common max-pool on the basis that in the temporal representation of a phase value, lower values correspond to earlier spikes. In biological networks, earlier spikes would result from stronger synaptic inputs and would more likely contribute to the later processing while later spikes may be ignored or canceled (29). Min-pooling also may be possible

to approximate based on a combination of winner-take-all circuits and network dynamics (30). We find that the substitution of a min-pool operation for max-pool operation in the Phasor CIFAR networks leads to no significant change in performance. However, average pooling leads to significant performance loss and is not used.

Both network types (standard and phasor) are trained using an augmented dataset to prevent overfitting. A rotation range of 15° , a width and height shift range of 10%, and 50% chance of a horizontal flip were used. All networks were trained using 70312 batches of 128 augmented images, corresponding approximately to 180 epochs on the original training dataset.

We found that in case of this more complex network architecture, no significant difference is observed between the standard and phasor networks' performance on the test set (Figure 2c). This contrasts with performance differences observed in the MNIST and FashionMNIST tasks, and may be due to the higher regularization penalties imposed on both networks and the more complex image recognition task. The kernel weight regularization may effectively penalize the standard network more than the phasor network with the same parameters, as it can be observed impacting standard network loss more in later epochs (Figure 2b) and the accuracy of the phasor networks on the original CIFAR-10 training set is significantly higher (Figure 2d).

To summarize, these results demonstrate that applying phasor-based representation and using the phasor neuron described in Equations 2-3 can create networks which achieve results on-par with standard networks. Some differences in performance between phasor and standard networks can be attributed to many factors, including the image-phase conversion method, regularization techniques, and the dataset. Next, we investigate an alternate inference mode for phasor networks which is inherently temporal in nature.

Temporal Evaluation

Equivalent Resonate and Fire Model

The key advantage of a phasor neuron is that its computations can be carried out approximately in the temporal domain, when all the information is not known *a priori* but instead arrives to the network at different times and in the form of binary spikes.

Taking a derivative of a complex number z representing a harmonic signal with respect to time (Equation 1) gives Equation 8, which is identical to the case of a resonate and fire (R&F) neuron with no 'leakage' (attraction to the rest state) (31). Leakage can be re-introduced and it shows that the dynamics of the R&F neuron are innately linked to the activation function forming the basis of inference in a phasor network. In the model of an R&F neuron with no leakage, the voltage-current oscillation produced after a current pulse is identical to the rotation of a phasor with respect to time represented in Equation 1. Following the original R&F convention, we refer to the 'current' U of an R&F neuron as the real part of its complex potential z , and its 'voltage' V as the imaginary part of z (31).

$$\text{Equation 7. } z = Ae^{i\omega t + \varphi}$$

$$\text{Equation 8. } \frac{\partial z}{\partial t} = (0 + i\omega)z \rightarrow (-b + i\omega)z$$

With this approach, the superposition and phase detection which was previously calculated atemporally using Equations 1-2 can be carried out exactly in the temporal domain using an R&F neuron with no leakage. First, the duration of one cycle of time in the system is defined as T , giving the neuron a natural

angular frequency ω of $2\pi/T$. Phases of an input vector \mathbf{x} are represented by Dirac delta functions which occur once per cycle. The amount by which this spike is offset from the temporal midpoint of the period is set proportionally to its value (e.g. an x of -1 is represented by a spike at the beginning of the period, and an x of 1 a spike at the end). Essentially, a spike represents the ‘peak’ of its original sinusoidal signal. Real-valued weights are represented again with \mathbf{w} (Equation 9).

$$\text{Equation 9.} \quad \frac{\partial z}{\partial t} = i\omega z + \sum_{i=1}^n \mathbf{w}_i \delta(t - x_i)$$

$$\text{Equation 10.} \quad z(T) = \sum_{i=1}^n \mathbf{w}_i \cdot e^{-i\pi x_i} \quad \text{if } z(0) = 0$$

Integrating Equation 9 through a single cycle ($t=0$ to 2 if $T = 2$) produces another form of the superposition of complex values (Equation 10, proof in methods). The timing of the inputs x defines the phase of the output z , which can be detected after the integration period by determining the time when two conditions (such as $V > 0$ and $\partial V/\partial t = 0$) are met. This allows the full calculation required for a Phasor neuron (complex superposition & phase measurement) to be carried out in the temporal domain using input spikes.

However, leakage must be retained within R&F neurons if they are to carry out different computations through time (allowing their potentials to gradually return to the initial condition required in Equation 10). By increasing the level of leakage b in the R&F neuron from 0, the same approximate calculation can be carried out, ideally without having a major effect on the phase of the superposition. Too high a leakage value will cause the ‘memory’ of the neuron to be too short, leaving it unable to calculate an approximation of Equation 10 as the resulting oscillations will decay too quickly to superimpose. However, too low a leakage value will prevent the neuron from returning to a rest state which is required to allow it to adapt flexibly to new computations through time. To strike a balance between these extremes, we use a leakage set to $1/5^{\text{th}}$ the value of the integration period T (Table 1).

The representation of an input spike by an instantaneous Dirac delta function at a time x can be relaxed by convolving it with a kernel such as a box function ($\Pi(t)$ with width scale factor s). These alterations (leakage and box kernel) are included in Equation 11, which is solved numerically through time to calculate the complex potential z of a Phasor neuron. To reiterate the other parameters in this equation, T is the R&F neuron’s fundamental period, b is a positive value which sets the neuron’s leakage, \mathbf{w} is the vector of the neuron’s n real-valued input weights, and t is time. In Table 1 we present the values used for these parameters in our experiments.

$$\text{Equation 11.} \quad \frac{\partial z}{\partial t} = \left(-b \cdot T + \frac{i2\pi}{T}\right) z + \sum_{i=1}^n \mathbf{w}_i \Pi(s \cdot t - x_i)$$

The spiking threshold of an R&F neuron is an important parameter. To meet the requirements of a phasor network, a spike is produced from the R&F neuron when it reaches a certain phase of its current/voltage oscillation. This phase can be found by determining when the neuron’s complex potential sweeps through a defined set of conditions. Here we define a set of conditions which causes the R&F neuron to produce a spike: (a) its imaginary value (voltage) reaches a maximum, i.e. $\partial \text{Im}(Z)/\partial t = 0$ and (b) has a positive imaginary value $\text{Im}(Z) > 0$; (c) its voltage is above a set threshold ($\text{Im}(Z) > V_{th}$), and (d) the time after last preceding spike exceeds refractory period ($T/4$). The last condition reduces the occurrence of multiple spikes in the same period. This gradient-based method allows the output spikes to be sparsely produced without referencing an external clock. For conciseness and given their approximate equivalence, we term an R&F neuron using this spike detection method as a temporal phasor neuron.

Table 1: Parameters used for temporal phasor neurons.

Parameter	Value
Period (T)	1.0 s
Leakage (b)	0.2
Box width scale (s)	0.05
Threshold (V_{th})	0.03
Refractory Period	0.25 s

Demonstration of Equivalent Neuron

Next, we first demonstrate that a temporal phasor neuron can carry out the identity function: given an input consisting of binary spikes repeating once a period, a phasor neuron resonates with this stimulus to produce another series of output spikes (Figure 1a-b, d-e). To communicate the phase of an input, these spikes are offset from the center of an interval relative to their value (e.g. if $x = [-1, 0, 1]$ and $T = 1$, $t = [0, \frac{1}{2}, 1], [1, \frac{3}{2}, 2], \dots$).

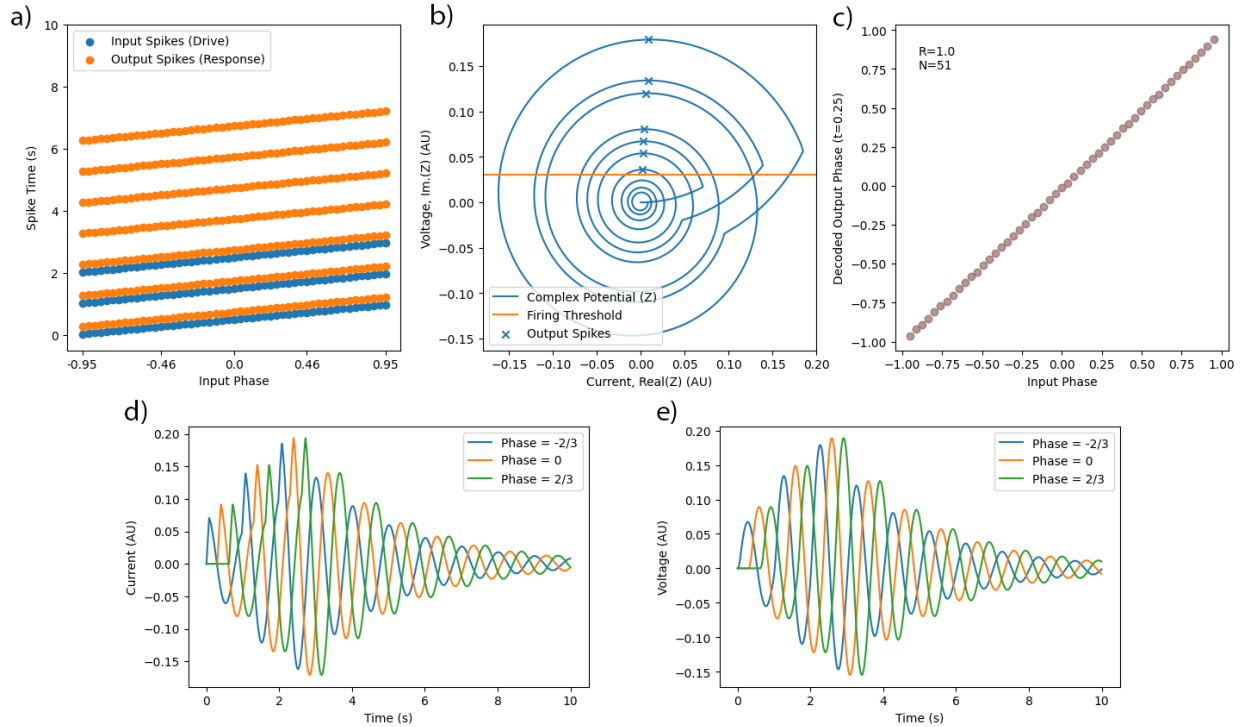


Figure 3: (a) A Phasor neuron is stimulated by an input spike train with different phases relative to the absolute start time $t=0$ s. (b) The arrival of these impulses spaced with the neuron's period cause it to resonate as it integrates the current resulting from the spike, firing once a cycle when it reaches its maximum voltage level. (c) The phase of the neuron's output spikes can be decoded using the initial starting time plus an integration delay (0.25 s). These decoded phases match the input phases to a high degree of precision. The difference in dynamics created by phase offsets can be clearly seen here by comparing the currents (d) and voltages (e) of a Phasor neuron.

Each stage of integration produces a quarter-period of delay ($T/4$) relative to its input. Adding this delay relative to the absolute time reference of the network's starting point, the phases of the output spikes can be decoded and compared to the ideal values encoded within the input spike trains. These decoded output phases successfully reproduce the values encoded in the input (Figure 3c). This result shows that the complex summation and phase-detection can succeed at integrating and replicating a single input.

However, the superposition of multiple inputs being calculated correctly through time is not addressed here, and is evaluated in the next section.

Demonstration of Equivalent Layer

To demonstrate that a temporal phasor neuron can calculate an approximately correct superposition of its inputs (as described in Equation 11), we create a series of neurons corresponding to a ‘layer’ in a conventional network. The input weights to this temporal layer are identical to those found in the hidden layer of an atemporal Phasor network after it was trained on the standard MNIST dataset. A series of stimuli consisting of random phases applied to each neuron are constructed and evaluated using the atemporal and temporal methods. The conversions between spikes and phases at each layer inputs and outputs are identical to what we previously described. However, as each neuron is operating temporally, it is now a subject to spikes from multiple (784) sources and it has to accurately integrate the weighted sum of these inputs to produce a correctly-timed output spike (Figure 4a-b).

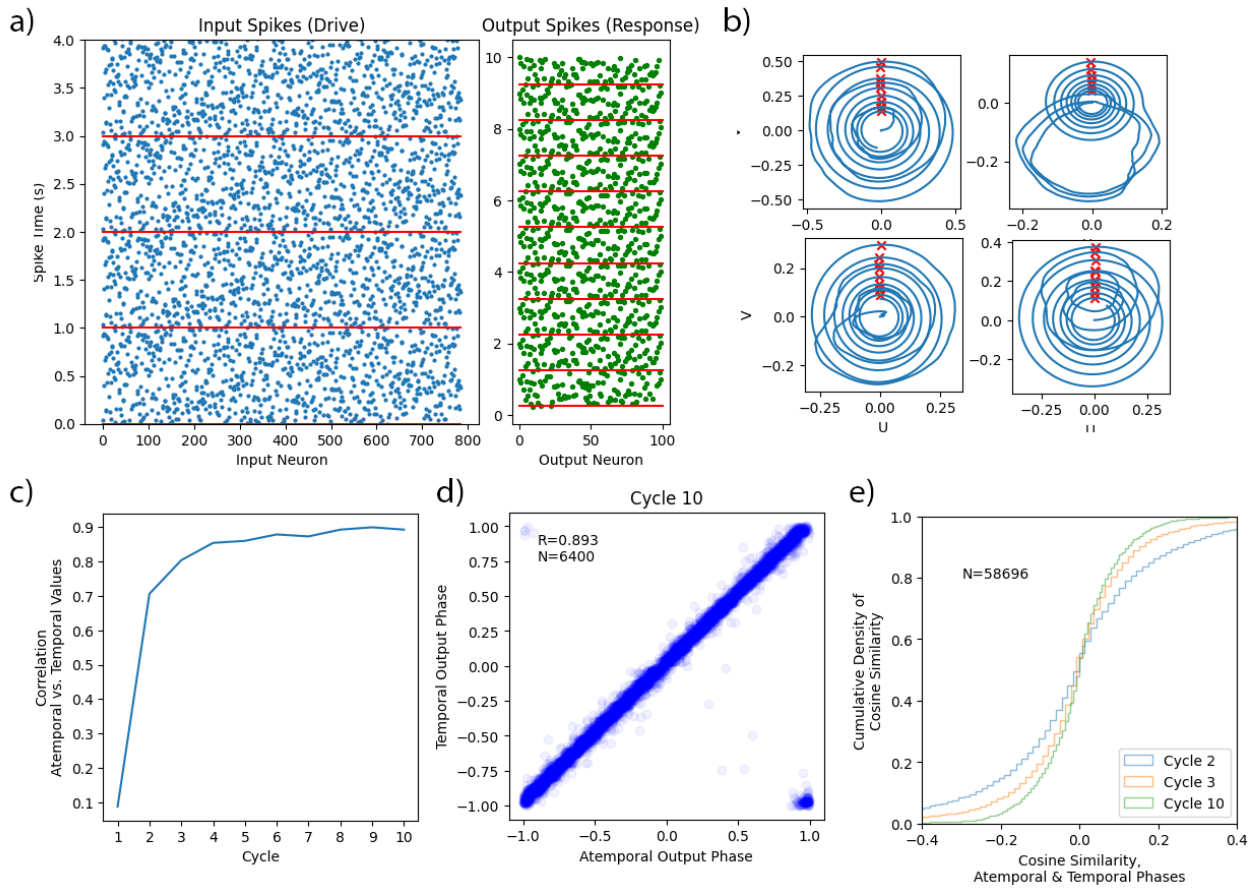


Figure 4: (a) A spike raster shows 1 set of 64 inputs which stimulate a layer of Phasor neurons that produces a series of spikes in response. Horizontal red lines demarcate the boundaries between integration periods. (b) Phase portraits of individual Phasor neurons being driven show their integration of multiple inputs into a complex value which evolves with time and produces an output spike at a single phase. All current (U) and voltage (V) values in arbitrary units. (c) After several periods of integration, the spike phases decoded from the temporal network using an absolute time reference and the ideal values produced by the atemporal network are highly correlated. (d,e) The cosine similarity between the temporal and atemporal phases shows the error produced by the temporal evaluation, which decreases with integration time.

Results are summarized in Figure 4. Importantly, the approximations used in Equation 11 (i.e., introduction of leakage and box kernel) do not prevent a temporal Phasor neuron from producing a value

which is highly correlated to its atemporal value ($R=0.89$ in the final integration period) (Figure 4c-e). This demonstrates that a temporally-executed layer of Phasor neurons can produce a good approximation of its atemporal counterpart.

Demonstration of Equivalent Network

Given the approximate equivalence of a phasor layer executing via spikes in the temporal domain, next we tested performance of the full networks used for image classification tasks. These networks were created identically to networks demonstrated in the atemporal experiments: both the MLP and convolutional networks were trained in the atemporal domain using standard backpropagation to reduce the loss function described in Equation 5. However, instead of executing by passing tensors of real values from layer to layer (atemporal execution), here the networks execute by sending precisely-timed binary spikes between layers (temporal execution). Network weights remain identical between execution modes.

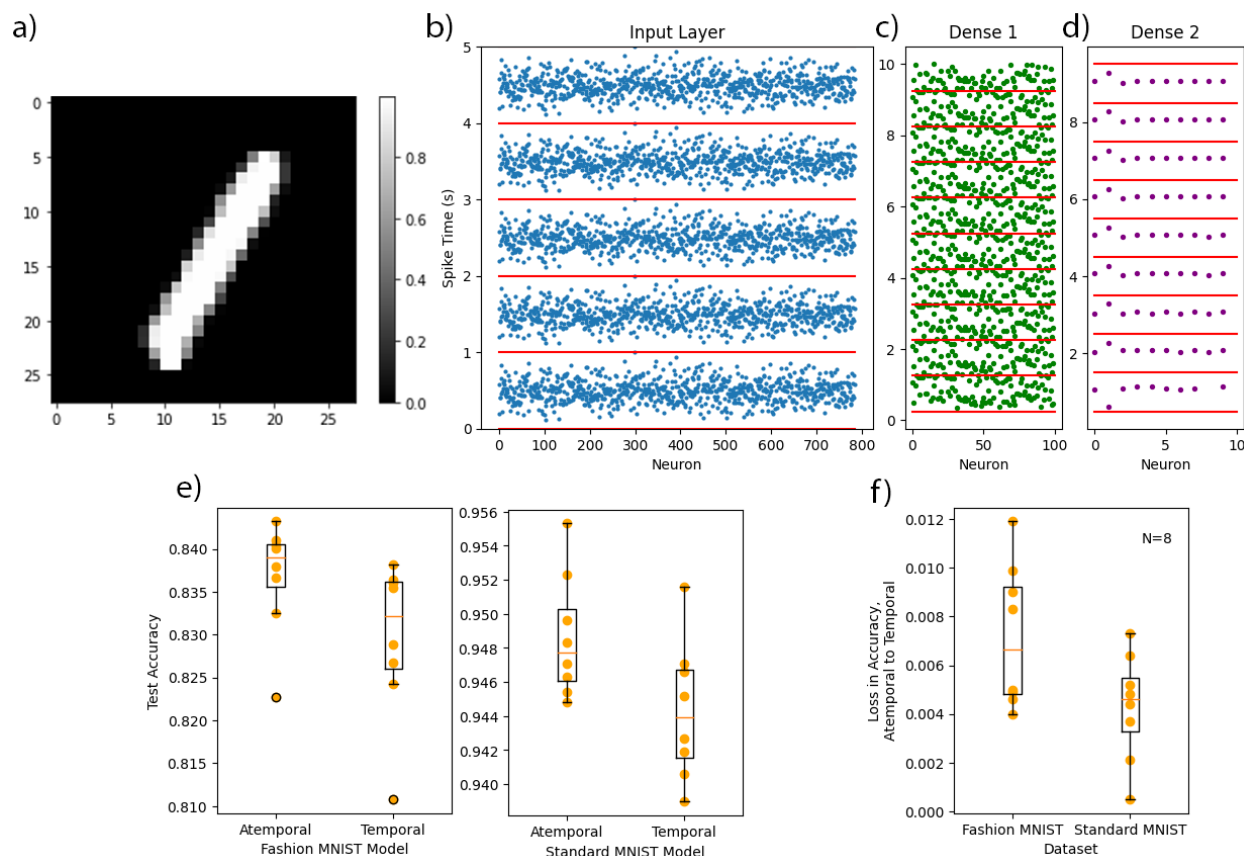


Figure 5: (a) An input image from the MNIST dataset of the digit '1'. This image is (1) converted from intensities to phases and (2) into a spike train (b) which drives the phasor network in the temporal domain (c). Horizontal red lines demarcate the boundaries between integration periods. The network has been trained to produce an out-of-phase spike on the image label ('1', d). (e) 2 sets of 8 networks trained on the MNIST and FashionMNIST datasets are evaluated in both their atemporal and temporal execution methods, and the resulting accuracies on the test set are reported. (f) Running in temporal evaluation mode, most models lost an average of only 0.57% accuracy compared to atemporal evaluation.

Inputs to the networks are provided by stimulating the input layer with a series of spikes encoding the phase into their relative timing as previously described. These input impulses repeat every cycle during the execution of the network (Figure 5b).

The predicted output class of an image is decoded from the output spike train by detecting the phase of spikes produced during the output layer's last full execution cycle (i.e. the final full cycle before the simulation's stopping time is reached). The phase is decoded by referencing to the initial start time, and the predicted label is defined by the neuron with the phase closest to the target value of $\frac{1}{2}$ (Figure 5d).

We find that despite the significant change in underlying execution strategy – from standard matrix multiplication and activation function to the integration of spike-driven currents and phase detection through time – the final accuracy differs little between the MLP networks (Figure 5f). After an input image is flattened and converted to spike trains, each spiking layer of the network can perform an integration through time with sufficiently high accuracy to produce the desired output (Figure 5a-d). Results from 2 sets of 8 networks trained on the standard MNIST or Fashion MNIST datasets show that the two execution modes are very similar and, on average, only 0.57% accuracy is lost by switching from atemporal to temporal execution (Figure 5e-f).

Next, a phasor-based convolutional network was executed temporally to test consequences of having a wider and deeper network architecture when using the temporal execution method. To temporally execute the min-pool operation, spikes within the pooling groups were examined cycle-to-cycle, and the earliest spike time in the pool was selected to be output. Due to greater resources required to simulate the temporal execution of this network with 70,514 neurons (versus 110 for the previous networks), a smaller test set of 1024 images was used. Running a single network on this reduced CIFAR test set, the network reached accuracies of 71.4% and 73.5% for temporal and atemporal execution modes, respectively. This corresponds to 2.1% accuracy loss by switching to the temporal execution mode.

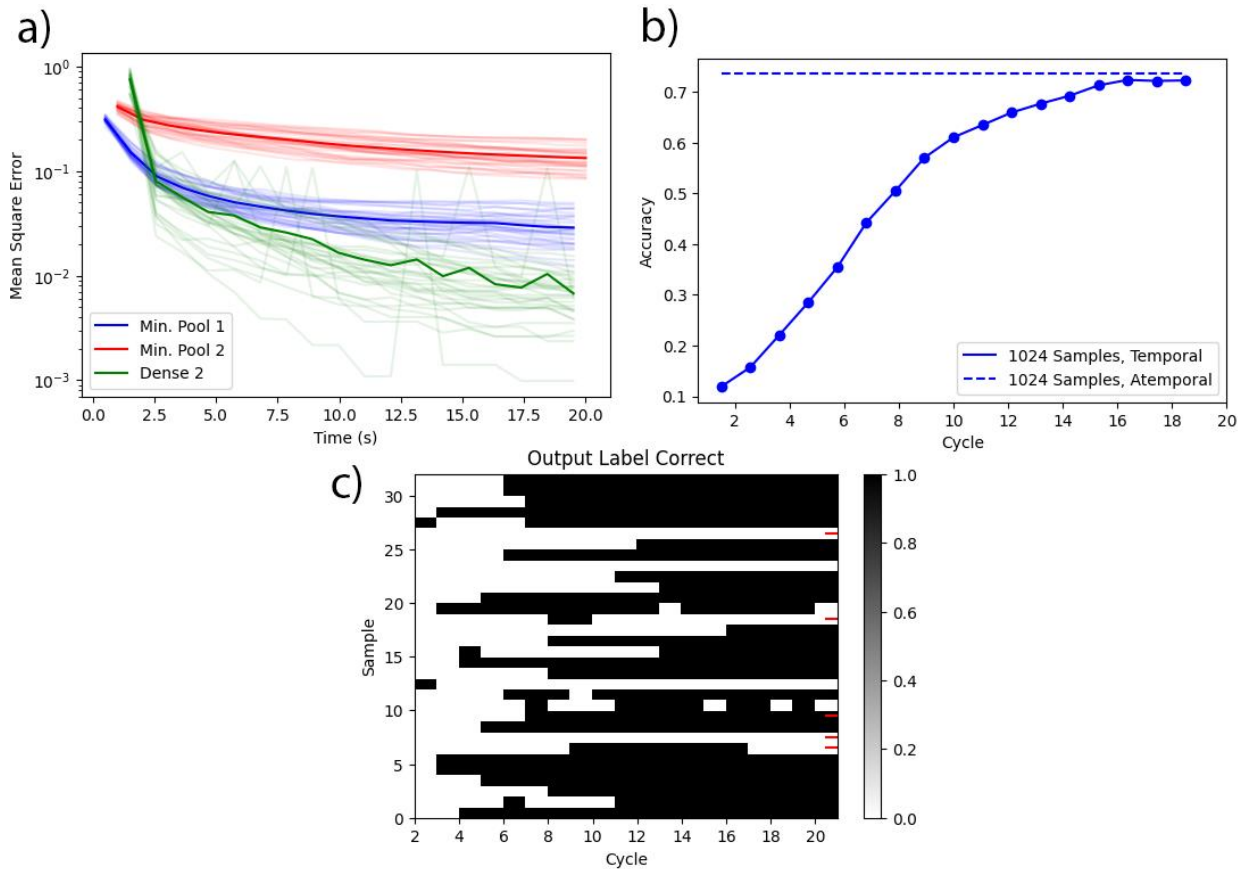


Figure 6: (a) The mean squared error of phases produced by the temporal CIFAR network is computed by decoding the phases represented by temporal spikes and comping these values to those produced by atemporal execution. Results are presented from the outputs of the convolutional and dense blocks. Information propagates quickly from layer to layer, initially decaying more than exponentially. (b) The accuracy of the labels decoded at the spiking output with respect to time is plotted against the static accuracy for the given sample set. Within 15 execution cycles, the CIFAR network can reach an accuracy comparable to its static counterpart. (c) The correctness of decoded output labels with respect to time is shown, with each image corresponding to a row. Some images quickly reach the correct output, and others require more time for error within the network to be reduced. As expected, images misclassified under atemporal execution (marked with red ticks on the right side) are more likely to be misclassified under dynamic execution as well.

The greater depth and width of the network used for CIFAR data set allows to examine in more details the propagation of information through the layers with respect to time. This was measured by calculating the mean squared error (MSE) between the phase encoded by spikes in the network and the phases calculated in the network under atemporal execution. We find that the initial execution cycles lead to the largest decreases in MSE, which continue to decay in time as more spikes propagate forward (Figure 6a). Different layers reach different lower bounds in error, and these differences stem from the approximate integration carried out by the resonate-and-fire neuron. A low error (approximately 1% MSE) is required at the dense output layer in order to reach classification performance comparable to atemporal execution (Figure 6b). As the temporal execution network approximates the same calculations carried out under atemporal execution, misclassified images are usually shared between execution modes (Figure 6c).

Discussion

In this study, we showed that the real valued activation function of a standard artificial neural network can be replaced by one that represents the angle of a complex value, or ‘phasor’. With this approach, each

neuron in the network integrates the phases of a set of inputs and generates a new output phase, which then propagates to the next layers. If all inputs are known ahead of time and with high precision, this calculation can be done in a time-agnostic or ‘atemporal’ manner. However, if all inputs are not known ahead of time, the calculation can also be carried out in real-time, integrating the signals as they arrive to produce a dynamic, time-varying calculation. In the former case, values are communicated via tensors of real values, and in the latter case, communications are carried out using spikes. We believe that this model brings deep learning closer to biological relevance while maintaining key advantages over other spike-based deep learning models.

Execution

One of the important advantages of phasor representation is its ability to present the network with a complete input within a set time interval defined by the neuron’s resonant frequency; each phase is encoded by the spike timing (its offset within the defined interval) and not by the accumulated rate of spikes (as is the case in rate-coding). This allows the network to produce outputs much more efficiently (as shown in Figure 5b) and on an established time basis, rather than only after waiting an arbitrarily defined amount of time. Additionally, the dynamic coupling between layers transmits information through the network with small delays, although time is required for the temporal outputs to reach a high degree of precision. Further latency characteristics still need to be tested, as well as the performance of phasor networks in modern, very deep networks with real-world applications such as image detectors (32).

An argument which can be presented against temporal phasor networks is that they trade off the long integration times of rate-based networks by instead using a continuous time domain which may consist of an equivalent or even greater number of discrete steps when calculated on digital, clocked hardware. This is a salient point which must be addressed by future work which examines in more depth the effect of time and weight quantization on the execution of phasor networks. However, even if using an equivalent number of time steps, phase-based encoding maintains the advantage that only one spike is required per integration period and all values are encoded with an equal amount of error, in contrast to rate-based coding which may require many spikes and encodes different values with different amounts of uncertainty (9,20).

The oscillatory dynamics inherent in the temporal processing of a Phasor neuron offers the possibility that the required calculations could be implemented efficiently via a variety of novel analog hardware devices specifically designed to carry out computations via coupled oscillators (33). These devices can exploit the natural dynamics of electrical or mechanical oscillations to compute with extremely high efficiency. Combining these two approaches could therefore offer a potential application for new emerging systems by providing a framework for executing traditional AI methods with high efficiency via coupled oscillations.

It may be possible to implement phasor networks on several current neuromorphic platforms; however, many of these platforms use integrate-and-fire dynamics, rather than resonate-and-fire or more complex models (5,34,35). However, previous work by Frady et al. (23) has demonstrated how resonate-and-fire networks can be implemented via network dynamics based on integrate-and-fire neurons, providing a possible method to extend Phasor networks to execute via simpler neuronal dynamics.

Training & Architecture

Another challenge of neuromorphic, spike-based architectures is the problem of how they can be efficiently trained *in-situ*, rather than exist solely as inference-only conversions of conventional networks trained via standard backpropagation on traditional hardware. This complex challenge consists of many issues, both practical and theoretical. Two of the foremost practical issues include backpropagating errors

through binary spikes and the high memory requirements of training methods (such as backpropagation through time (BPTT)) which address the recurrent, temporal nature of spiking networks (36,37).

The use of surrogate gradients to produce eligibility traces on synapses allows synaptic variables to be included as a part of a dynamical system solved forward through time, allowing an observer in the future to approximately infer how recent spikes contributed to the current neuronal state and assign error credit (36,38). But rather than using traditional BPTT to solve credit assignment with a phasor network, its continuous update may allow instead for adjoint sensitivity methods to solve the coupled system backwards in time for a short period (39). This would greatly reduce the memory requirements of assigning credit through time, potentially creating an efficient method for training phasor networks inherently in the temporal domain. Future work could also investigate the application of synaptic plasticity, local learning rules, and feedback alignment in phasor networks to avoid the larger problems of gradient and weight transport (36,40).

Lastly, the fundamental representation of information via phase values in this network provides a rich basis of computation which can allow future phasor networks to compute with radically different architectures than traditional networks. This is due to the fact that a vector of phase values as used in the networks is identical to the basis of information in a vector-symbolic architecture, the Fourier Holographic Reduced Representation (FHRR) (41,42). This enables vectors produced by each layer of a phasor network to be manipulated through vector-symbolic manipulations such as binding and bundling, allowing rich data structures to be built within the framework of the network's evaluation (43). These operations can be used to build new generation computation architectures with capabilities such as the factorization of components into symbols, linking them to the emerging field of neurosymbolic computation while maintaining spike-compatible computation (44,45).

Conclusion

We demonstrated that by replacing the activation function of a standard feed-forward network by one created via complex operations, a novel 'phasor' network may be designed that can be executed either temporally or atemporally with no conversion process and only slight differences in output. The spiking and oscillatory computations of the temporal Phasor network have strong parallels to biological computation, can be adapted to current or future neuromorphic hardware, and provide a rich basis for the construction of novel training methods and architectures.

References

1. Schwartz R, Dodge J, Smith NA, Etzioni O. Green AI. *Commun ACM*. 2020;63(12):54–63.
2. Sucholutsky I, Schonlau M. ‘Less than one’-shot learning: Learning N classes from $M < N$ samples. *arXiv [Internet]*. 2020; Available from: <http://arxiv.org/abs/2009.08449>
3. van de Ven GM, Tolias AS. Three scenarios for continual learning. 2019;1–18. Available from: <http://arxiv.org/abs/1904.07734>
4. Marcus G. The next decade in AI: Four steps towards robust artificial intelligence. *arXiv*. 2020;(February).
5. Schuman CD, Potok TE, Patton RM, Birdwell JD, Dean ME, Rose GS, et al. A Survey of Neuromorphic Computing and Neural Networks in Hardware. 2017;1–88. Available from: <http://arxiv.org/abs/1705.06963>
6. Thakur CS, Molin J, Cauwenberghs G, Indiveri G, Kumar K, Qiao N, et al. Large-Scale Neuromorphic Spiking Array Processors: A quest to mimic the brain. *arXiv*. 2018;12(December):1–37.
7. Christensen D V., Dittmann R, Linares-Barranco B, Sebastian A, Gallo M Le, Redaelli A, et al. 2021 Roadmap on Neuromorphic Computing and Engineering. 2021; Available from: <http://arxiv.org/abs/2105.05956>
8. Diehl PU, Neil D, Binas J, Cook M, Liu SC, Pfeiffer M. Fast-classifying, high-accuracy spiking deep networks through weight and threshold balancing. *Proc Int Jt Conf Neural Networks*. 2015;2015-Septe.
9. Rueckauer B, Lungu IA, Hu Y, Pfeiffer M, Liu SC. Conversion of continuous-valued deep networks to efficient event-driven networks for image classification. *Front Neurosci*. 2017 Dec 7;11(DEC).
10. Wu D, Yi X, Huang X. A Little Energy Goes a Long Way: Energy-Efficient, Accurate Conversion from Convolutional Neural Networks to Spiking Neural Networks. 2021; Available from: <http://arxiv.org/abs/2103.00944>
11. Cessac B, Paugam-Moisy H, Viéville T. Overview of facts and issues about neural coding by spikes. *J Physiol Paris [Internet]*. 2010;104(1–2):5–18. Available from: <http://dx.doi.org/10.1016/j.jphysparis.2009.11.002>
12. Thorpe S, Fize D, Marlot C. Speed of processing in the human visual system. *Nature*. 1996;381(6582):520–2.
13. Panzeri S, Diamond ME. Information carried by population spike times in the whisker sensory cortex can be decoded without knowledge of stimulus time. *Front Synaptic Neurosci*. 2010;2(JUN):1–14.
14. Quian Quiroga R, Panzeri S. Extracting information from neuronal populations: Information theory and decoding approaches. *Nat Rev Neurosci*. 2009;10(3):173–85.
15. Tiesinga P, Fellous JM, Sejnowski TJ. Regulation of spike timing in visual cortical circuits. *Nat Rev Neurosci*. 2008;9(2):97–107.
16. Ward-Foxton S. Intel Benchmarks Neuromorphic Chip Against AI Accelerators. *EE Times*

- [Internet]. 2020 Dec; Available from: <https://www.eetimes.com/intel-benchmarks-neuromorphic-chip-against-ai-accelerators/>
17. Stöckl C, Maass W. Optimized spiking neurons classify images with high accuracy through temporal coding with two spikes. 2020;1–23. Available from: <http://arxiv.org/abs/2002.00860>
 18. Rueckauer B, Liu SC. Conversion of analog to spiking neural networks using sparse temporal coding. *Proc - IEEE Int Symp Circuits Syst.* 2018;2018-May:0–4.
 19. Kheradpisheh SR, Masquelier T. Temporal Backpropagation for Spiking Neural Networks with One Spike per Neuron. *Int J Neural Syst.* 2020;30(6).
 20. Davidson S, Furber SB. Comparison of Artificial and Spiking Neural Networks on Digital Hardware. *Front Neurosci.* 2021;15(April):1–7.
 21. Davies M, Wild A, Orchard G, Sandamirskaya Y, Guerra GAF, Joshi P, et al. Advancing Neuromorphic Computing With Loihi: A Survey of Results and Outlook. *Proc IEEE.* 2021;
 22. Noest AJ. Discrete-state phasor neural networks. *Phys Rev A.* 1988;38(4):2196–9.
 23. Frady EP, Sommer FT. Robust computation with rhythmic spike patterns. *Proc Natl Acad Sci U S A.* 2019;116(36):18050–9.
 24. Hecht E. *Optics.* Pearson Education; 2017.
 25. Lecun Y, Bengio Y, Hinton G. Deep learning. *Nature.* 2015;521(7553):436–44.
 26. LeCun Y, Cortes C, Burges CJ. MNIST handwritten digit database. ATT Labs [Online] Available <http://yann.lecun.com/exdb/mnist>. 2010;2.
 27. Xiao H, Rasul K, Vollgraf R. Fashion-MNIST: A novel image dataset for benchmarking machine learning algorithms. *arXiv.* 2017. p. 1–6.
 28. Krizhevsky A, Hinton G, others. Learning multiple layers of features from tiny images. 2009;
 29. Imam N, Cleland TA. Rapid online learning and robust recall in a neuromorphic olfactory circuit. *arXiv [Internet].* 2019;2(March):181–91. Available from: <http://dx.doi.org/10.1038/s42256-020-0159-4>
 30. Lynch N, Musco C, Parter M. Winner-Take-All Computation in Spiking Neural Networks. 2019;1–94. Available from: <http://arxiv.org/abs/1904.12591>
 31. Izhikevich EM. Resonate-and-fire neurons. *Neural Networks.* 2001;14(6–7):883–94.
 32. Tan M, Pang R, Le Q V. EfficientDet: Scalable and Efficient Object Detection. 2020;10778–87.
 33. Csaba G, Porod W. Coupled oscillators for computing: A review and perspective. *Appl Phys Rev.* 2020;7(1).
 34. Davies M, Srinivasa N, Lin T-H, Chinya G, Cao Y, Choday SH, et al. Loihi: A neuromorphic manycore processor with on-chip learning. *IEEE Micro.* 2018;38(1):82–99.
 35. Akopyan F, Sawada J, Cassidy A, Alvarez-Icaza R, Arthur J, Merolla P, et al. TrueNorth: Design and Tool Flow of a 65 mW 1 Million Neuron Programmable Neurosynaptic Chip. *IEEE Trans Comput Des Integr Circuits Syst.* 2015;34(10):1537–57.

36. Neftci EO, Mostafa H, Zenke F. Surrogate Gradient Learning in Spiking Neural Networks. 2019;1–25. Available from: <http://arxiv.org/abs/1901.09948>
37. Goodfellow I, Bengio Y, Courville A. Deep Learning [Internet]. MIT Press; 2016. (Adaptive computation and machine learning). Available from: <https://books.google.com/books?id=Np9SDQAAQBAJ>
38. Bellec G, Scherr F, Subramoney A, Hajek E, Salaj D, Legenstein R, et al. A solution to the learning dilemma for recurrent networks of spiking neurons. *Nat Commun.* 2020;11(1).
39. Chen RTQ, Rubanova Y, Bettencourt J, Duvenaud D. Neural Ordinary Differential Equations. *ArXiv.* 2018;109(NeurlPS):31–60.
40. Zenke F, Neftci EO. Brain-Inspired Learning on Neuromorphic Substrates. *Proc IEEE.* 2021;1–16.
41. Schlegel K, Neubert P, Protzel P. A comparison of Vector Symbolic Architectures. 2020; Available from: <http://arxiv.org/abs/2001.11797>
42. Plate TA. Holographic reduced representations. *IEEE Trans Neural networks.* 1995;6(3):623–41.
43. Neubert P, Schubert S, Protzel P. An Introduction to Hyperdimensional Computing for Robotics. *KI - Künstliche Intelligenz [Internet].* 2019;33(4):319–30. Available from: <https://doi.org/10.1007/s13218-019-00623-z>
44. Frady EP, Kent S, Olshausen BA, Sommer FT. Resonator networks for factoring distributed representations of data structures. 2020;1–20. Available from: <http://arxiv.org/abs/2007.03748>
45. Garcez A d’Avila, Lamb LC. Neurosymbolic AI: The 3rd Wave. 2020;1–36. Available from: <http://arxiv.org/abs/2012.05876>

Materials & Methods

Code Availability

Networks were created and executed under Python 3.8.5 with Tensorflow 2.4.1 and SciPy 1.4.0. The full environment and all code/parameters necessary to generate figures are included in a public GitHub repository (https://github.com/wilkieolin/phasor_networks).

Proof of Equation 10

$$\frac{\partial z}{\partial t} = i\omega z + \sum_{i=1}^n w_i \delta(t - x_i)$$
$$z(T) = \int_0^2 i\omega z + \sum_{i=1}^n w_i \delta(t - x_i) \partial t$$

Given the assumptions:

1. An initial condition $z(t = 0) = 0$.
2. The previous bounds $x \in [-1,1]$ are shifted to $x \in [0,2]$ by adding 2 to all elements of x less than zero. This is equivalent to offsetting traditional radian-based values by 2π , leading to an identical phase.
3. The elements of x are unique and sorted in ascending order.

$$z(T) = \int_0^2 \sum_{i=1}^n w_i \delta(t - x_i) \partial t$$

The first term is removed given the initial condition and the integration is performed only over the summation of currents. The element x_1 will have the lowest value and thus be the first delta function to be ‘activated’ with respect to time.

$$z(x_1^+) = \int_0^{x_1^+} w_1 \delta(t - x_1) + \sum_{n=2}^n w_i \delta(t - x_i) \partial t$$
$$z(x_1^+) = w_1 \cdot 1 = w_1 e^{i\pi 0}$$

This contribution in the real domain represents the ‘current’ from synapse i which arrives at phase x . The sinusoidal oscillation between current and voltage in the R&F neuron is handled through the first term of the update equation which now has a non-zero value.

$$z(x_2^+) = \int_{x_1^+}^{x_2^+} i\omega z(x_1^+) + \sum_{n=2}^n w_i \delta(t - x_i) \partial t$$
$$z(x_2^+) = w_1 e^{i\pi(x_2 - x_1)} + w_2 e^{i\pi 0}$$

By induction, the following sum at $t=2$ is produced:

$$z(2) = \sum_{i=1}^n w_i e^{i\pi(2 - x_i)} = \sum_{i=1}^n w_i e^{-i\pi x_i}$$